Journal Pre-proofs

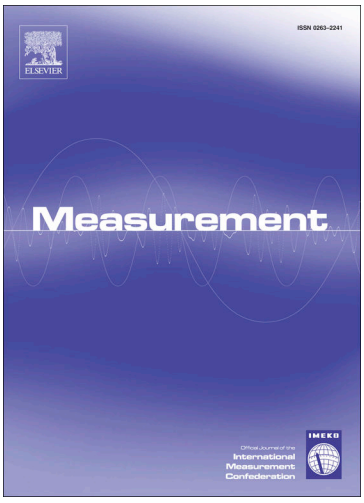

Underwater two-way acoustic and pressure gauge fusion navigation algorithm utilizing optimal constraints and smoothing

Yangfan Liu, Jaume Sanz Subirana, Tianhe Xu, Junting Wang, Wenfeng Nie, Jianxu Shu

PII: S0263-2241(25)01944-X
DOI: https://doi.org/10.1016/j.measurement.2025.118585
Reference: MEASUR 118585

To appear in: *Measurement*

Received Date: 14 May 2025
Revised Date: 25 July 2025
Accepted Date: 28 July 2025

Please cite this article as: Y. Liu, J.S. Subirana, T. Xu, J. Wang, W. Nie, J. Shu, Underwater two-way acoustic and pressure gauge fusion navigation algorithm utilizing optimal constraints and smoothing, *Measurement* (2025), doi: https://doi.org/10.1016/j.measurement.2025.118585

Underwater Two-Way Acoustic and Pressure Gauge Fusion Navigation Algorithm Utilizing Optimal Constraints and Smoothing

1. Yangfan Liu

liuyangfan1995@163.com

Institute of Space Science, Shandong University, Weihai, China

Research group of Astronomy and Geomatics (gAGE), Universitat Politècnica de Catalunya (UPC), Barcelona, Spain

2. Jaume Sanz Subirana

jaume.sanz@upc.edu

Research group of Astronomy and Geomatics (gAGE), Universitat Politècnica de Catalunya (UPC), Barcelona, Spain

3. Tianhe Xu

Corresponding author

thxu@sdu.edu.cn

Institute of Space Science, Shandong University, Weihai, China

4. Junting Wang

wjtsci2015@163.com

Institute of Space Science, Shandong University, Weihai, China

5. Wenfeng Nie

wenfengnie@sdu.edu.cn

Institute of Space Science, Shandong University, Weihai, China

6. Jianxu Shu

shujx@mail.sdu.edu.cn

Institute of Space Science, Shandong University, Weihai, China

CRediT authorship contribution statement

Yangfan Liu: Conceptualization, Methodology, Software, Formal analysis, Writing - original draft, Writing - review & editing. **Jaume Sanz Subirana**: Conceptualization, Review & editing, Supervision. **Tianhe Xu**: Conceptualization, Review & editing, Supervision, Project administration, Funding acquisition. **Junting Wang**: Conceptualization, Formal analysis, Validation, Visualization. **Wenfeng Nie**: Validation, Visualization. **Jianxu Shu**: Validation, Visualization.

Declaration of competing interest

The authors declare that they have no known competing financial interests or personal relationships that could have appeared to influence the work reported in this paper.

Data availability

The data supporting the results of this study are not publicly accessible due to the regulatory policies of the relevant organizations. However, the data can be obtained from the corresponding author upon reasonable request.

Highlights

1. A detailed functional model of underwater acoustic two-trip navigation is proposed.

2. A method to search for the optimal constraint information using PDOP is developed.

3. A depth-constrained ray tracing method is constructed in underwater navigation.

4. A depth constraint method based on coordinate system transformation is presented.

Underwater Two-Way Acoustic and Pressure Gauge Fusion Navigation Algorithm Utilizing Optimal Constraints

Abstract: Underwater long baseline acoustic navigation system is widely used for underwater vehicle navigation. However, traditional methods exhibit a significant increase in the navigation error of the vehicle when the acoustic observation data quality is poor. To address this issue, we propose an underwater acoustic two-way navigation algorithm that incorporates depth constraint and Rauch-Tung-Striebel (RTS) smoothing. Specifically, the proposed algorithm derives a detailed function model for underwater acoustic two-way navigation. Additionally, the position dilution of precision (PDOP) is used to search for optimal constraint information. This constraint information is then integrated into the sound velocity calculation, and the vertical coordinate of the vehicle is constrained in the measurement equation. Finally, the RTS smoother is applied to smooth the constrained acoustic navigation results backward. Experiments conducted on high-quality data demonstrate that the proposed algorithm outperforms traditional methods with an average decrease of 4.42% in the three-dimensional root mean square (RMS-3D) value of the navigation errors. For the low-

quality data, the proposed algorithm shows an average reduction of 85.47% in the RMS-3D value in contrast to traditional methods. These results suggest that the proposed algorithm exhibits superior accuracy and stability compared to traditional methods, especially in the up direction.

Keywords: acoustic two-way navigation; extended Kalman filter; navigation function model; PDOP; depth constraint; RTS smoothing

1. Introduction

Underwater navigation has emerged as a crucial technology for ocean exploration, supporting various marine activities, including submarine seismic risk assessment, ocean crustal deformation, oceanographic surveying, and offshore exploration [1],[2]. The development trajectory of underwater navigation technology has undergone substantial evolution, driven by expanding research demands and practical applications in diverse marine exploration and operational scenarios [3]. Early underwater navigation predominantly relied on inertial navigation systems (INS). However, INS systems suffer from cumulative errors due to sensor drift and biases [4]. To mitigate these limitations, acoustic navigation methods, notably long baseline (LBL), short baseline (SBL), and ultra-short baseline (USBL) systems, were developed. LBL systems provide absolute positioning over long distances. SBL and USBL systems offer greater operational flexibility [5]. Subsequent advancements have focused on integrating multiple navigation techniques to enhance robustness and precision [6]. Hybrid navigation approaches now fuse acoustic positioning data with Doppler velocity logs (DVL), pressure gauges (PG), magnetometers, and occasionally surface-linked global navigation satellite systems (GNSS) data. These sensor integrations have been significantly augmented by sophisticated signal processing algorithms [7]. Data acquisition methodologies have concurrently advanced. These advancements include the incorporation of high-resolution sensors and comprehensive environmental monitoring parameters, such as temperature, salinity, pressure, and sound velocity profiles. Together, these improvements support more accurate acoustic propagation modeling. The evolution in underwater communication technologies, particularly acoustic modems and communication systems, has substantially improved data transmission efficiency [8]. These communication enhancements have facilitated improved operational planning, rapid data processing, and enhanced coordination of multi-vehicle systems. Collectively, these progressive developments highlight an ongoing research trajectory dedicated to refining navigation accuracy, robustness, and adaptability for complex marine environments [9].

LBL acoustic navigation system is a commonly used method in underwater navigation, known for its high navigation accuracy and extensive operational range [10]. This navigation system comprises of a transducer installed on the bottom of underwater vehicle and transponders anchored to the seafloor [11],[12]. Typically, four or more transponders are used, and they are precisely calibrated to ensure accurate positioning [13]. The principle of LBL acoustic navigation involves the transducer transmitting the inquiry acoustic signal, which is then received by the transponder and responded with an acoustic signal [14]. The transducer subsequently receives the response acoustic signal, as shown in Fig. 1 [15],[16]. Through this process, the acoustic propagation time between the transducer and the transponder is determined. Combined with the sound velocity profile, the observation distance from the transducer to the transponder can then be calculated [17]. The Kalman filter is then employed to facilitate the navigation of the underwater vehicle [18]. The complexity of the marine environment makes acoustic observation data vulnerable to various error factors, which leads to a decrease in data quality [19],[20]. Consequently, the navigation error of underwater vehicles increases significantly [21],[22].

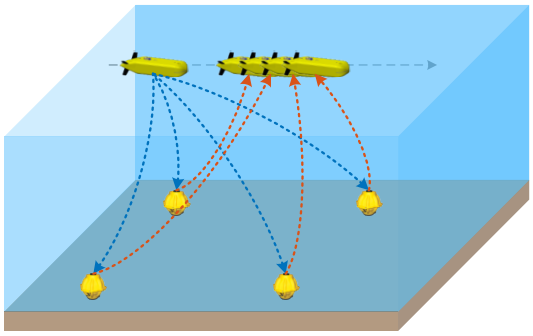

Fig. 1. A schematic diagram of the two-way LBL system.

To enhance the navigation accuracy of underwater vehicle, many approaches have been proposed in recent years. Costanzi et al. proposed a navigation strategy based on an unscented Kalman filter specifically for autonomous underwater vehicle (AUV) and experimentally verified it. The results demonstrate the effectiveness of the selected strategy, producing satisfactory accuracy in vehicle position estimation [23]. Wang et al. introduced an acoustic navigation approach that utilizes unscented Kalman filtering. This method applies unscented transformation to estimate the system state vector and its covariance matrix, reducing the linearization error of the measurement equation. Additionally, the approach employs Sage-Husa filtering based on innovation vectors to adaptively adjust the measurement noise [24]. Shu et al. developed a method to address the issue of dynamic model mismatch in underwater acoustic navigation. The approach constructed mixed equivalent variances through multiple models and incorporated them into each model to achieve interactive robust estimation [25]. Wang et al. utilized the wavelet transform and the Fourier transform to construct a system error correction model in acoustic positioning. They further incorporated the estimated systematic errors into acoustic navigation to enhance the accuracy of acoustic navigation observations [26]. Yang et al. introduced a robust observation model incorporating periodic error parameters. By leveraging the systematic errors present in the residual series, they applied a piecewise second-order polynomial to model the residuals. This model is used to mitigate the impact of measurement distance error in underwater acoustic navigation [27]. Qin et al. developed an advanced resilient model that accounts for both temporal and spatial variations in sound velocity errors to estimate spatiotemporal sound velocity errors. They subsequently utilize the estimated sound velocity error in LBL acoustic navigation [28]. Cao et al. proposed a travel-time processing scheme for LBL systems that identifies and excludes large travel-time outliers and accounts for vehicle motion during asynchronous acoustic signal reception. This method enabled centimeter-level positioning accuracy in simulations and demonstrated robust performance in deep-sea AUV field trials [29]. Huang et al. introduced an adaptive extended Kalman filter (AEKF) for cooperative AUV localization. This filter adaptively estimates the predicted error covariance and measurement noise parameters online using an expectation-maximization algorithm. As a result, it effectively addresses the challenge of unknown or time-varying noise conditions [30]. Furthermore, Huang et al. developed an outlier-resilient Gaussian approximate filter based on the heavy-tailed Student's t distribution. This filter suppresses the adverse effects of spurious velocity and range measurements in cooperative AUV localization. This robust filtering technique achieved superior localization accuracy and robustness in lake trials [31].

The methods described above have been effective in reducing the influence of factors such as gross error, dynamic model, and system error on LBL acoustic navigation. As a result, the navigation accuracy of the underwater vehicle is improved. However, these methods still result in a significant increase in the navigation error when the acoustic data quality is poor due to the partial loss of the acoustic observation signal.

To address the above issue, we propose an underwater acoustic two-way navigation algorithm that incorporates depth constraint and Rauch-Tung-Striebel (RTS) backward smoothing. Firstly, a rigorous function model of underwater

acoustic two-way navigation is established based on the principle of LBL acoustic navigation. Additionally, the sound velocity and the vertical coordinate of the vehicle are constrained by making for the information of the pressure gauge and the position dilution of precision (PDOP). Finally, to account for the large process noise inherent in the process model and the part of unmodeled system errors that are classified as measurement noise, the RTS smoothing algorithm is utilized to perform backward smoothing on the navigation results.

The proposed algorithm presents the main contributions that can be summarized as follows:

1) A detailed function model of underwater acoustic round trip navigation is provided, which is more consistent with the "inquiry-response-reception" mode of underwater acoustic navigation. This approach reduces navigation error caused by the model.

2) We developed a deep constraint method based on coordinate system transformation and used PDOP to search for the optimal constraint information. This approach can enhance the accuracy and reliability of the constraint information, resulting in more precise navigation.

3) To improve distance measurement accuracy and reduce navigation error, the constraint information is extended to not only constrain the calculation of sound velocity but also the vertical coordinate of the vehicle in the Cartesian coordinate system.

The remainder of this paper is organized as follows. The related works for underwater acoustic navigation are presented in Section 2. In Section 3, we describe the proposed algorithm in detail. The experiments and analysis are reported in Section 4. Finally, some conclusions are drawn in Section 5.

2. Preliminaries

This section outlines the theoretical basis for the proposed algorithm. It begins with a detailed function model for underwater two-way positioning, followed by an introduction to an effective smoothing algorithm.

2.1. The function model for underwater acoustic two-way positioning

The seafloor transponder's position is determined by the intersection of distances calculated using acoustic signals [32]. In the "inquiry-response-reception" mode of underwater acoustic signal propagation, the vehicle's position differs at the time of signal emission and reception [33],[34]. As a result, a function model for underwater acoustic two-way positioning is presented as

$$\rho_i = f(\boldsymbol{X}_i^{d-}, \boldsymbol{X}^p) + f(\boldsymbol{X}_i^{d+}, \boldsymbol{X}^p) + \delta\rho_i^v + \delta\rho_i^t + \varepsilon_i \tag{1}$$

where i represents the index of the i-*th* epoch; $\boldsymbol{X}_i^{d-}$ and $\boldsymbol{X}_i^{d+}$ are the coordinates of the vehicle at the acoustic signal emission and reception, respectively; $\boldsymbol{X}^p$ denotes the unknown coordinate of the transponder; $\delta\rho_i^v$ and $\delta\rho_i^t$ are the ranging errors caused by the sound velocity error and the time delay error, respectively; ε_i represents the measurement noise in the ranging process; ρ_i denotes the measured two-way distance between the vehicle and the transponder; $f(\boldsymbol{X}_i^{d-}, \boldsymbol{X}^p)$ and $f(\boldsymbol{X}_i^{d+}, \boldsymbol{X}^p)$ refer to the theoretical geometric distances between the vehicle and transponder at the times of signal emission and reception, respectively.

The geometric distance at the signal emission in Eq. (1) can be expressed as

$$f(\boldsymbol{X}_i^{d-}, \boldsymbol{X}^p) = \sqrt{(x_i^{d-} - x^p)^2 + (y_i^{d-} - y^p)^2 + (z_i^{d-} - z^p)^2} \tag{2}$$

where $\boldsymbol{X}_i^{d-} = (x_i^{d-}, y_i^{d-}, z_i^{d-})^T$ is the coordinate of the vehicle at the acoustic signal emission, $\boldsymbol{X}^p = (x^p, y^p, z^p)^T$ represent the coordinate of the transponder.

Furthermore, we can express the geometric distance at the signal reception using the same formula.

2.2. The smoothing algorithm

RTS smoothing algorithm is a recursive Bayesian filtering technique used for state-optimal smoothing in dynamic systems [35]. The algorithm is a fixed-interval smoother that combines current measurements with previous estimates to estimate the true state of the system [36].

The RTS enhances the precision of estimates by introducing a smoothing step to the Kalman filter. The algorithm commences by retaining the information obtained during forward Kalman filtering, followed by the execution of the smoothing algorithm in reverse order of measurements [37]. The process of the RTS can be outlined as follows.

Algorithm Procedure of the RTS

Input: The state transition matrix $\boldsymbol{\Phi}_{i/i-1}$, the state estimation vector $\hat{\boldsymbol{X}}_{f,i}$, the state estimation covariance matrix $\boldsymbol{P}_{f,i}$, the state prediction vector $\hat{\boldsymbol{X}}_{f,i/i-1}$, the state prediction covariance matrix $\boldsymbol{P}_{f,i/i-1}$, they are obtained during forward Kalman filtering.

Output: $\hat{\boldsymbol{X}}_{s,i}$ and $\boldsymbol{P}_{s,i}$, $i = n-1, n-2, \mathrm{L}\ ,1$

1 **Initialize:** The initial value of the state estimation vector for backward smoothing $\hat{\boldsymbol{X}}_{s,n} = \hat{\boldsymbol{X}}_{f,n}$, the initial value of the state estimation covariance matrix for backward smoothing $\boldsymbol{P}_{s,n} = \boldsymbol{P}_{f,n}$.

2 **For** $i = n-1:-1:1$

3 $\boldsymbol{K}_{s,i} = \boldsymbol{P}_{f,i}\boldsymbol{\Phi}_{i+1/i}^{\mathrm{T}}\boldsymbol{P}_{f,i+1/i}^{-1}$ // the smoothing gain matrix

4 $\hat{\boldsymbol{X}}_{s,i} = \hat{\boldsymbol{X}}_{f,i} + \boldsymbol{K}_{s,i}(\hat{\boldsymbol{X}}_{s,i+1} - \hat{\boldsymbol{X}}_{f,i+1/i})$ // the state estimation vector

5 $\boldsymbol{P}_{s,i} = \boldsymbol{P}_{f,i} + \boldsymbol{K}_{s,i}(\boldsymbol{P}_{s,i+1} - \boldsymbol{P}_{f,i+1/i})\boldsymbol{K}_{s,i}^{\mathrm{T}}$ // the state estimation covariance matrix

6 **End for**

The RTS possesses the advantage of necessitating less storage information and demonstrating rapid calculation speed. Furthermore, it provides a more accurate and dependable estimation of the system in the presence of significant noise and measurement delay [38].

3. Methodology

The proposed algorithm aims to address the large navigation error in traditional methods when the acoustic data quality is poor due to the partial loss of the acoustic observation signals. To this end, we proposed an underwater acoustic two-way navigation algorithm that incorporates depth constraint and smoothing. The main contributions of the proposed

algorithm are as follows: 1) establishing a function model for underwater two-way navigation in the local Cartesian coordinate system; 2) developing depth constraints based on coordinate system transformation and PODP; 3) constraining the calculation of equivalent sound velocity and measurement solutions. These three contributions are crucial for improving navigation accuracy. Consequently, the relevant details of these three contributions and the overall process of the proposed algorithm are outlined below. The main symbols and notations used are presented in Table 1.

Table 1 List of main symbols and notations.

Symbol	Explanation
$\boldsymbol{X}$	State parameter vector
$\boldsymbol{\Phi}$	State transition matrix
$\boldsymbol{\Gamma}$	Process noise allocation matrix
$\boldsymbol{W}$	Process noise vector
$\boldsymbol{V}$	Velocity vector
$\boldsymbol{A}$	Acceleration vector
$\boldsymbol{Y}$	Vehicle coordinate in the local Cartesian coordinate system
Δt	Time interval between consecutive epochs at the signal emission
$\boldsymbol{I}$	Identity matrix
$\boldsymbol{Z}$	Innovation vector
$\boldsymbol{H}$	Jacobian matrix
$\boldsymbol{\varepsilon}$	Comprehensive error term
h	Ellipsoid height

H	Normal height
ξ	Elevation anomaly
d	Draft of the underwater vehicle (positive value)
$\boldsymbol{U}$	Vehicle coordinate in the geodetic coordinate system
$\boldsymbol{J}$	Coordinate transformation from the geodetic coordinate system to the local Cartesian coordinate system
$\boldsymbol{L}$	Coordinate transformation from the local Cartesian coordinate system to the geodetic coordinate system
$\boldsymbol{Q}$	Cofactor matrix
$\boldsymbol{G}$	Geometry matrix
C_e	Constrained two-way equivalent sound velocity
g	Gradient of the sound velocity profile
θ	Incident angle
p	Snell constant

3.1. The function model for the underwater two-way navigation

In underwater acoustic navigation, traditional methods do not distinguish between one-way and two-way modes. They also neglect the discrepancies in the vehicle's position at signal transmission and reception, as well as the variations in vehicle's position at each instance of signal reception. These omissions introduce systematic deviations into the function model, as illustrated in Fig. 1. To address this limitation, a more rigorous two-way navigation function model is developed. The construction of the function model for underwater acoustic two-way navigation within the local Cartesian coordinate system involves several steps.

Firstly, in the constant acceleration (CA) process model, the state transition matrix is established based on the time difference between adjacent epochs at the acoustic signal emission. The predicted position of the vehicle at the acoustic signal emission can be estimated as

$$\boldsymbol{X}_{i/i-1} = \boldsymbol{\Phi}_{i/i-1}\boldsymbol{X}_{i-1} + \boldsymbol{\Gamma}_{i/i-1}\boldsymbol{W}_{i-1} \tag{3}$$

$$\boldsymbol{X}_{i/i-1}=\left[\boldsymbol{Y}_i^{0d-}\quad \boldsymbol{V}_i^0\quad \boldsymbol{A}_i^0\right]^T \tag{4}$$

$$\boldsymbol{\Phi}_{i/i-1}=\begin{bmatrix}\boldsymbol{I}_{3*3} & \boldsymbol{M}_1 & \boldsymbol{M}_2\\ \boldsymbol{0}_{3*3} & \boldsymbol{I}_{3*3} & \boldsymbol{M}_1\\ \boldsymbol{0}_{3*3} & \boldsymbol{0}_{3*3} & \boldsymbol{I}_{3*3}\end{bmatrix} \tag{5}$$

$$\boldsymbol{M}_1=\begin{bmatrix}\Delta t_{i/i-1} & 0 & 0\\ 0 & \Delta t_{i/i-1} & 0\\ 0 & 0 & \Delta t_{i/i-1}\end{bmatrix} \tag{6}$$

$$\boldsymbol{M}_2=\begin{bmatrix}\Delta t_{i/i-1}^2/2 & 0 & 0\\ 0 & \Delta t_{i/i-1}^2/2 & 0\\ 0 & 0 & \Delta t_{i/i-1}^2/2\end{bmatrix} \tag{7}$$

$$\boldsymbol{X}_{i-1}=\left[\boldsymbol{Y}_{i-1}^{d-}\quad \boldsymbol{V}_{i-1}\quad \boldsymbol{A}_{i-1}\right]^T \tag{8}$$

$$\boldsymbol{\Gamma}_{i/i-1}=\left[\boldsymbol{M}_2\quad \boldsymbol{M}_1\quad \boldsymbol{I}_{3*3}\right]^T \tag{9}$$

$$\boldsymbol{W}_{i-1}=\left[w_{i-1}^e\quad w_{i-1}^n\quad w_{i-1}^u\right]^T \tag{10}$$

where $i/i-1$ is the transition from the *i-1-th* epoch to the *i-th* epoch; $\boldsymbol{X}_{i/i-1}$ and $\boldsymbol{X}_{i-1}$ are the state prediction and estimation vectors, respectively; $\boldsymbol{Y}_i^{0d-}=(e_i^{0d-},n_i^{0d-},u_i^{0d-})$ and $\boldsymbol{Y}_{i-1}^{d-}=(e_{i-1}^{d-},n_{i-1}^{d-},u_{i-1}^{d-})$ are the predicted and estimated positions of the vehicle within the local Cartesian coordinate system at the acoustic signal emission, respectively; $\boldsymbol{V}_i^0=(v_i^{0e},v_i^{0n},v_i^{0u})$ and $\boldsymbol{V}_{i-1}=(v_{i-1}^e,v_{i-1}^n,v_{i-1}^u)$ are the predicted and estimated velocities of the vehicle at the acoustic signal emission, respectively; $\boldsymbol{A}_i^0=(a_i^{0e},a_i^{0n},a_i^{0u})$ and $\boldsymbol{A}_{i-1}=(a_{i-1}^e,a_{i-1}^n,a_{i-1}^u)$ are the predicted and estimated accelerations of the vehicle at the acoustic signal emission, respectively; $\boldsymbol{\Phi}_{i/i-1}$ is the state transition matrix; $\boldsymbol{\Gamma}_{i/i-1}$ is the process noise allocation matrix; $\Delta t_{i/i-1}$ is the time interval between consecutive epochs at the acoustic signal emission; $\boldsymbol{W}_{i-1}$ is the process noise of acceleration.

The state prediction value at the signal reception is then determined using the time interval between the acoustic signal emission and reception, which means

$$\boldsymbol{Y}_{ij}^{0d+}=\left[\boldsymbol{I}_{3*3}\quad \boldsymbol{M}_3\quad \boldsymbol{M}_4\right]\left[\boldsymbol{Y}_i^{0d-}\quad \boldsymbol{V}_i^0\quad \boldsymbol{A}_i^0\right]^T \tag{11}$$

$$\boldsymbol{M}_3=\begin{bmatrix}\Delta t_{ij}^{er} & 0 & 0\\ 0 & \Delta t_{ij}^{er} & 0\\ 0 & 0 & \Delta t_{ij}^{er}\end{bmatrix} \tag{12}$$

$$\boldsymbol{M}_4=\begin{bmatrix}(\Delta t_{ij}^{er})^2/2 & 0 & 0\\ 0 & (\Delta t_{ij}^{er})^2/2 & 0\\ 0 & 0 & (\Delta t_{ij}^{er})^2/2\end{bmatrix} \tag{13}$$

where j represents the index of the j-*th* transponder; $\boldsymbol{Y}_{ij}^{0d+}=(e_{ij}^{0d+},n_{ij}^{0d+},u_{ij}^{0d+})^T$ is the predicted position of the vehicle within the local Cartesian coordinate system at the acoustic signal reception, Δt_{ij}^{er} denotes the time interval between the acoustic signal emission and reception.

Finally, the Jacobian matrix of the function model is calculated through the Taylor series expansion method. The resulting function model is presented as

$$\boldsymbol{Z}_i=\boldsymbol{H}_i\delta\boldsymbol{X}_i+\boldsymbol{\varepsilon}_i \tag{14}$$

$$\boldsymbol{Z}_i=\begin{bmatrix}\rho_{i1}-f_{i1}^{0-}-f_{i1}^{0+}\\ \rho_{i2}-f_{i2}^{0-}-f_{i2}^{0+}\\ \mathrm{M}\\ \rho_{im}-f_{im}^{0-}-f_{im}^{0+}\end{bmatrix} \tag{15}$$

$$\boldsymbol{H}_i=\begin{bmatrix}\boldsymbol{H}_i^{pos} & \boldsymbol{H}_i^{vel} & \boldsymbol{H}_i^{acc}\end{bmatrix} \tag{16}$$

$$\boldsymbol{H}_i^{pos}=\begin{bmatrix}\frac{\partial f_{i1}^{0-}}{\partial e_i^{d-}}+\frac{\partial f_{i1}^{0+}}{\partial e_i^{d-}} & \frac{\partial f_{i1}^{0-}}{\partial n_i^{d-}}+\frac{\partial f_{i1}^{0+}}{\partial n_i^{d-}} & \frac{\partial f_{i1}^{0-}}{\partial u_i^{d-}}+\frac{\partial f_{i1}^{0+}}{\partial u_i^{d-}}\\ \frac{\partial f_{i2}^{0-}}{\partial e_i^{d-}}+\frac{\partial f_{i2}^{0+}}{\partial e_i^{d-}} & \frac{\partial f_{i2}^{0-}}{\partial n_i^{d-}}+\frac{\partial f_{i2}^{0+}}{\partial n_i^{d-}} & \frac{\partial f_{i2}^{0-}}{\partial u_i^{d-}}+\frac{\partial f_{i2}^{0+}}{\partial u_i^{d-}}\\ \mathrm{M} & \mathrm{M} & \mathrm{M}\\ \frac{\partial f_{im}^{0-}}{\partial e_i^{d-}}+\frac{\partial f_{im}^{0+}}{\partial e_i^{d-}} & \frac{\partial f_{im}^{0-}}{\partial n_i^{d-}}+\frac{\partial f_{im}^{0+}}{\partial n_i^{d-}} & \frac{\partial f_{im}^{0-}}{\partial u_i^{d-}}+\frac{\partial f_{im}^{0+}}{\partial u_i^{d-}}\end{bmatrix} \tag{17}$$

$$\boldsymbol{H}_i^{vel}=\begin{bmatrix}\frac{\partial f_{i1}^{0+}}{\partial e_i^{d-}}\Delta t_{i1}^{er} & \frac{\partial f_{i1}^{0+}}{\partial n_i^{d-}}\Delta t_{i1}^{er} & \frac{\partial f_{i1}^{0+}}{\partial u_i^{d-}}\Delta t_{i1}^{er}\\ \frac{\partial f_{i2}^{0+}}{\partial e_i^{d-}}\Delta t_{i2}^{er} & \frac{\partial f_{i2}^{0+}}{\partial n_i^{d-}}\Delta t_{i2}^{er} & \frac{\partial f_{i2}^{0+}}{\partial u_i^{d-}}\Delta t_{i2}^{er}\\ \mathrm{M} & \mathrm{M} & \mathrm{M}\\ \frac{\partial f_{im}^{0+}}{\partial e_i^{d-}}\Delta t_{im}^{er} & \frac{\partial f_{im}^{0+}}{\partial n_i^{d-}}\Delta t_{im}^{er} & \frac{\partial f_{im}^{0+}}{\partial u_i^{d-}}\Delta t_{im}^{er}\end{bmatrix} \tag{18}$$

$$\boldsymbol{H}_i^{acc}=\begin{bmatrix}\frac{\partial f_{i1}^{0+}}{\partial e_i^{d-}}(\Delta t_{i1}^{er})^2/2 & \frac{\partial f_{i1}^{0+}}{\partial n_i^{d-}}(\Delta t_{i1}^{er})^2/2 & \frac{\partial f_{i1}^{0+}}{\partial u_i^{d-}}(\Delta t_{i1}^{er})^2/2\\ \frac{\partial f_{i2}^{0+}}{\partial e_i^{d-}}(\Delta t_{i2}^{er})^2/2 & \frac{\partial f_{i2}^{0+}}{\partial n_i^{d-}}(\Delta t_{i2}^{er})^2/2 & \frac{\partial f_{i2}^{0+}}{\partial u_i^{d-}}(\Delta t_{i2}^{er})^2/2\\ \mathrm{M} & \mathrm{M} & \mathrm{M}\\ \frac{\partial f_{im}^{0+}}{\partial e_i^{d-}}(\Delta t_{im}^{er})^2/2 & \frac{\partial f_{im}^{0+}}{\partial n_i^{d-}}(\Delta t_{im}^{er})^2/2 & \frac{\partial f_{im}^{0+}}{\partial u_i^{d-}}(\Delta t_{im}^{er})^2/2\end{bmatrix} \tag{19}$$

$$\begin{cases} \dfrac{\partial f_{ij}^{0-}}{\partial e_i^{d-}} = \dfrac{e_i^{0d-} - e_j^p}{f_{ij}^{0-}} & \dfrac{\partial f_{ij}^{0+}}{\partial e_i^{d-}} = \dfrac{e_i^{0d+} - e_j^p}{f_{ij}^{0+}} \\ \dfrac{\partial f_{ij}^{0-}}{\partial n_i^{d-}} = \dfrac{n_i^{0d-} - n_j^p}{f_{ij}^{0-}} & \dfrac{\partial f_{ij}^{0+}}{\partial n_i^{d-}} = \dfrac{n_i^{0d+} - n_j^p}{f_{ij}^{0+}} \\ \dfrac{\partial f_{ij}^{0-}}{\partial u_i^{d-}} = \dfrac{u_i^{0d-} - u_j^p}{f_{ij}^{0-}} & \dfrac{\partial f_{ij}^{0+}}{\partial u_i^{d-}} = \dfrac{u_i^{0d+} - u_j^p}{f_{ij}^{0+}} \end{cases} \tag{20}$$

$$\begin{cases} f_{ij}^{0-} = f(\boldsymbol{Y}_i^{0d-}, \boldsymbol{Y}_j^p) \\ f_{ij}^{0+} = f(\boldsymbol{Y}_{ij}^{0d+}, \boldsymbol{Y}_j^p) \end{cases} \tag{21}$$

$$\delta \boldsymbol{X}_i = (\boldsymbol{X}_i - \boldsymbol{X}_{i/i-1}) \tag{22}$$

$$\boldsymbol{\varepsilon}_i = \begin{bmatrix} \delta\rho_{i1}^v + \delta\rho_{i1}^t + \varepsilon_{i1} \\ \delta\rho_{i2}^v + \delta\rho_{i2}^t + \varepsilon_{i2} \\ \mathrm{M} \\ \delta\rho_{im}^v + \delta\rho_{im}^t + \varepsilon_{im} \end{bmatrix} \tag{23}$$

where m represents the number of transponder signals received by the vehicle at the epoch i; $\boldsymbol{Z}_i$ denotes the innovation vector; $\boldsymbol{H}_i$ represents the Jacobian matrix, $\boldsymbol{H}_i^{pos}$ denotes the Jacobian matrix related to the vehicle's position at the acoustic signal emission, while $\boldsymbol{H}_i^{vel}$ corresponds to its velocity and $\boldsymbol{H}_i^{acc}$ to its acceleration at that instant; $\delta \boldsymbol{X}_i$ represents the adjustment to the state predicted vector of the vehicle at the acoustic signal emission; $\boldsymbol{\varepsilon}_i$ denotes a comprehensive error term.

3.2. The depth constraints based on coordinate system transformation and PODP

The pressure gauge measures the vehicle's depth relative to the instantaneous sea level. Integrating pressure gauge data with underwater acoustic navigation supplies additional observations. These observations help compensate for the geometric configuration defects caused by partial signal loss. As a result, navigation accuracy is enhanced.

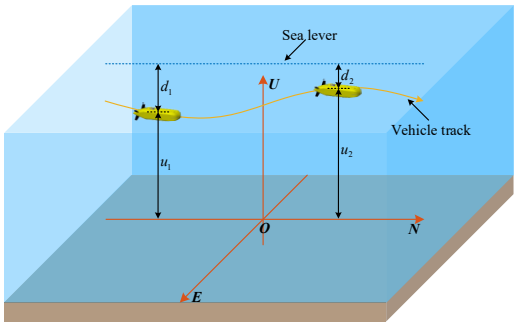

Fig. 2. A depth constraint diagram in the local Cartesian coordinate system within a small range.

Underwater acoustic navigation is usually conducted within the local Cartesian coordinate system, as shown in Fig. 2. Therefore, the depth constraint equation based on the pressure gauge in the local Cartesian coordinate system can be expressed as

$$u_1 + d_1 + \varepsilon_1 = u_2 + d_2 + \varepsilon_2 \tag{24}$$

where u_1 and u_2 are vertical coordinates of the vehicle at different times; d_1 and d_2 are vehicle's depth values at different times; ε_1 and ε_2 are random errors at different times.

Therefore, the parameters obtained at one epoch can be used to provide depth constraints for the coordinates at another. However, as the vehicle travels farther, the accuracy of Eq. (24) decreases due to the effects of Earth's curvature, as illustrated in Fig. 3.

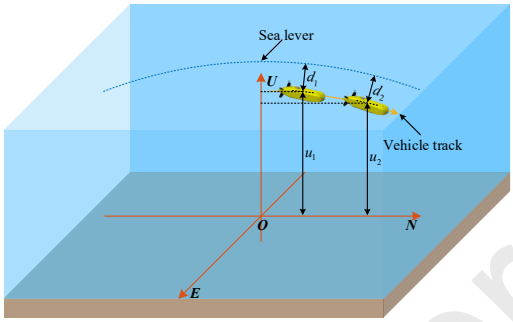

Fig. 3. A depth constraint diagram in the local Cartesian coordinate system over a large range.

According to the relationship between the reference ellipsoid and the quasi-geoid, it can be concluded that

$$h = H + \xi \tag{25}$$

where, h is the ellipsoid height; H is the normal height; ξ is the elevation anomaly.

In marine environments, the quasi-geoid and sea level are usually considered to be approximately equal, so that

$$H = -d \tag{26}$$

where, d is the draft of the underwater vehicle (positive value).

Substituting Eq. (26) into Eq. (25), we can obtain

$$h = -d + \xi \tag{27}$$

According to the above formula, if the geodetic height of the vehicle at a certain epoch is known, we can get

$$h^0 = -d^0 + \xi^0 \tag{28}$$

where, h^0 is the known geodetic height of the vehicle, d^0 and ξ^0 are the corresponding draft and elevation anomaly, respectively.

Subtracting Eq. (28) from Eq. (27) yields

$$h = h^0 + d^0 - \xi^0 - d + \xi \tag{29}$$

where, h is the geodetic height of the vehicle to be estimated; h^0 is the known geodetic height of the vehicle; d^0 and d are the draft, which can be obtained by pressure gauge measurement; ξ^0 and ξ are the elevation anomalies, which can be calculated by interpolation of the elevation anomaly grid product.

Underwater acoustic navigation is typically conducted in the local Cartesian coordinate system, while the depth constraint in Eq. (29) is formulated in the geodetic coordinate system. The process for depth constraints based on coordinate system transformation is as follows.

First, the known vehicle's coordinates expressed in the local Cartesian coordinate system are transformed into the geodetic coordinate system. Second, the coordinates of the vehicle to be estimated are likewise converted from the local Cartesian coordinate system to the geodetic coordinate system. Equation (29) is then applied to constrain the ellipsoidal height of the vehicle to be estimated. Next, the constrained coordinates are transformed back from the geodetic coordinate system to the local Cartesian coordinate system. Finally, the constrained vertical coordinate of the vehicle to be estimated is obtained in the local Cartesian coordinate system. Therefore, a coordinate transformation is required. The constrained vertical coordinate of the vehicle, incorporating the depth constraint in the local Cartesian coordinate system, can be expressed as

$$\begin{cases} \boldsymbol{U}^0 = \boldsymbol{L}(\boldsymbol{Y}^0) \\ \boldsymbol{U}_i^{0d-} = \boldsymbol{L}(\boldsymbol{Y}_i^{0d-}) \\ \boldsymbol{U}_i^{cd-}(3) = \boldsymbol{U}^0(3) + d^0 - \xi^0 - d_i + \xi_i \\ \boldsymbol{Y}_i^{cd-} = \boldsymbol{J}(\boldsymbol{U}_i^{cd-}) \\ u_i^c = \boldsymbol{Y}_i^{cd-}(3) \end{cases} \tag{30}$$

where u_i^c and d_i are the constrained vertical coordinate and draft of the vehicle at the acoustic signal emission, respectively; d^0 represents the known vehicle's draft; ξ^0 and ξ are the elevation anomalies, which can be calculated by interpolation of the elevation anomaly grid product; $\boldsymbol{Y}^0$ denotes the known vehicle's coordinate in the local Cartesian coordinate system; $\boldsymbol{U}$ is the vehicle's coordinate in the geodetic coordinate system; (3) denotes the third element of the vector; $\boldsymbol{J}$ represents the transformation of coordinates from the geodetic coordinate system to the local Cartesian coordinate system; $\boldsymbol{L}$ denotes the transformation of coordinates from the local Cartesian coordinate system to the geodetic coordinate system.

Equation (29) shows that a precise depth constraint can only be achieved after the optimal reference vehicle position has been identified. Exploiting the established relationship between the geometric configuration of an underwater acoustic navigation network and its navigation accuracy, we use PDOP metric to determine the optimality of the constraint information.

This is achieved by calculating PDOP from the coordinates of the vehicle and seafloor transponders, and compared with the previous optimal PDOP [39]. If the current PDOP is lower than the previous optimal PDOP, the optimal constraint information will be replaced with the current constraint information that includes the draft and coordinate of the vehicle at the acoustic signal emission. Otherwise, the next step is executed directly. The PDOP calculation formula is expressed as

$$PDOP = \sqrt{q_{xx} + q_{yy} + q_{zz}} \tag{31}$$

$$\boldsymbol{Q}=\left(\boldsymbol{G}^{T}\boldsymbol{G}\right)^{-1}=\begin{bmatrix} q_{xx} & q_{xy} & q_{xz} \\ q_{yx} & q_{yy} & q_{yz} \\ q_{zx} & q_{zy} & q_{zz} \end{bmatrix} \tag{32}$$

$$\boldsymbol{G}=\begin{bmatrix} \dfrac{x_i^{d-}-x_1^p}{f(\boldsymbol{X}_i^{d-},\boldsymbol{X}_1^p)} & \dfrac{y_i^{d-}-y_1^p}{f(\boldsymbol{X}_i^{d-},\boldsymbol{X}_1^p)} & \dfrac{z_i^{d-}-z_1^p}{f(\boldsymbol{X}_i^{d-},\boldsymbol{X}_1^p)} \\ \dfrac{x_i^{d-}-x_2^p}{f(\boldsymbol{X}_i^{d-},\boldsymbol{X}_2^p)} & \dfrac{y_i^{d-}-y_2^p}{f(\boldsymbol{X}_i^{d-},\boldsymbol{X}_2^p)} & \dfrac{z_i^{d-}-z_2^p}{f(\boldsymbol{X}_i^{d-},\boldsymbol{X}_2^p)} \\ \mathrm{M} & \mathrm{M} & \mathrm{M} \\ \dfrac{x_i^{d-}-x_m^p}{f(\boldsymbol{X}_i^{d-},\boldsymbol{X}_m^p)} & \dfrac{y_i^{d-}-y_m^p}{f(\boldsymbol{X}_i^{d-},\boldsymbol{X}_m^p)} & \dfrac{z_i^{d-}-z_m^p}{f(\boldsymbol{X}_i^{d-},\boldsymbol{X}_m^p)} \end{bmatrix} \tag{33}$$

$$f(\boldsymbol{X}_i^{d-},\boldsymbol{X}_j^p)=\sqrt{(x_i^{d-}-x_j^p)^2+(y_i^{d-}-y_j^p)^2+(z_i^{d-}-z_j^p)^2} \tag{34}$$

where $\boldsymbol{Q}$ represents the cofactor matrix; $\boldsymbol{G}$ denotes the geometry matrix; i represents the index of the i-*th* epoch; j denotes the index of the j-*th* transponder; m represents the number of transponder signals received by the vehicle at the epoch i; $\boldsymbol{X}_i^{d-}=(x_i^{d-},y_i^{d-},z_i^{d-})^T$ is the coordinate of the vehicle at the acoustic signal emission; $\boldsymbol{X}_j^p=(x_j^p,y_j^p,z_j^p)^T$ is the coordinate of the transponder; $f(\boldsymbol{X}_i^{d-},\boldsymbol{X}_j^p)$ refers to the geometric distances between the vehicle and transponder.

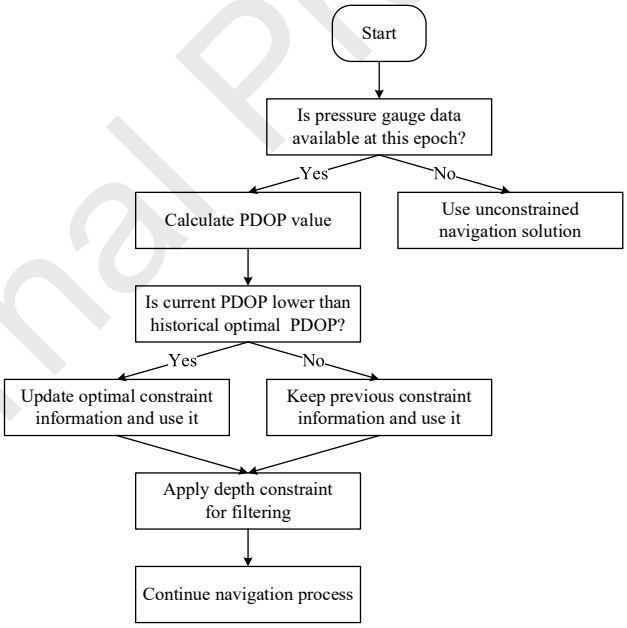

Fig. 4. A decision tree diagram for constraint condition selection.

3.3. The constraining of equivalent sound velocity and measurement solutions

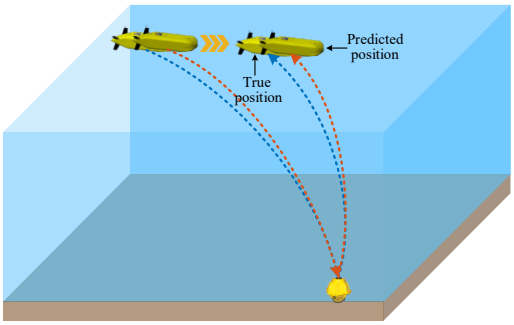

Fig. 5. A diagram of two-way equivalent acoustic ray tracing.

Because two spatially proximate vehicles receive acoustic signals that propagate along nearly identical ray paths from the same seafloor transponder (see Fig. 5), their associated propagation errors are highly correlated. Exploiting this feature, we propose a two-way equivalent acoustic ray tracing strategy, in which the effective sound velocity is determined based on the vehicle's predicted position. When the vehicle moves far from the transponder array, however, sound velocity related error and unfavorable geometric configuration significantly amplify the predicted positioning error in the vertical direction. Therefore, we impose a depth constraint on the predicted coordinates. Using these constrained coordinates, the acoustic ray tracing procedure is reapplied to obtain the two-way equivalent sound velocity, as expressed in Eq. (35).

$$\begin{cases} C_e = (C_e^- + C_e^+)/2 \\ C_e^- = \sqrt{\left(e^p - e^{cd-}\right)^2 + \left(n^p - n^{cd-}\right)^2 + \left(u^p - u^{cd-}\right)^2} \Big/ t^- \\ C_e^+ = \sqrt{\left(e^p - e^{cd+}\right)^2 + \left(n^p - n^{cd+}\right)^2 + \left(u^p - u^{cd+}\right)^2} \Big/ t^+ \end{cases} \tag{35}$$

where C_e denotes the constrained two-way equivalent sound velocity; $(e^{cd-}, n^{cd-}, u^{cd-})$ and $(e^{cd+}, n^{cd+}, u^{cd+})$ are the vehicle's constrained coordinates in the local Cartesian coordinate system at the signal emission and reception, respectively; (e^p, n^p, u^p) is the seafloor transponder's coordinate in the local Cartesian coordinate system; t^- and t^+ are the emission and reception propagation delays, obtained from the acoustic ray tracing algorithm.

The acoustic ray tracing algorithm can be described as

$$\begin{cases} t_k = \dfrac{1}{g_k} \ln\left(\tan\dfrac{\theta_{k+1}}{2} \Big/ \tan\dfrac{\theta_k}{2}\right) \\ y_k = \dfrac{\cos\theta_k - \cos\theta_{k+1}}{p g_k} \\ \mathrm{z}_k = \dfrac{\sin\theta_{k+1} - \sin\theta_k}{p g_k} \end{cases} \tag{36}$$

where k represents the index of the *k-th* layer of the sound speed profile; g_k is the gradient of the sound speed profile; θ_k is the incident angle; p is the Snell constant; t_k y_k and z_k are the acoustic propagation time, horizontal propagation distance, and vertical propagation distance, respectively.

The function model of two-way navigation is expanded by incorporating the constrained vertical coordinate of the vehicle at the acoustic signal emission, which enables the depth constraint into the measurement equation. Additionally, the

corresponding measurement noise is defined. The resulting constrained measurement equation is given as

$$\begin{bmatrix} \boldsymbol{Z}_i \\ \boldsymbol{Z}^c \end{bmatrix} = \begin{bmatrix} \boldsymbol{H}_i \\ \boldsymbol{H}^c \end{bmatrix} \delta \boldsymbol{X}_i + \begin{bmatrix} \boldsymbol{V}_i \\ \boldsymbol{V}^c \end{bmatrix} \tag{37}$$

where $\boldsymbol{Z}^c = u_i^c - u_i^{0d-}, u_i^{0d-}$ represents the predicted vertical coordinate of the vehicle at the acoustic signal emission; $\boldsymbol{H}^c = [0, 0, 1, 0, 0, 0, 0, 0, 0]$; $\boldsymbol{V}^c$ is the measurement noise of depth constraint.

3.4. The overall process of the proposed algorithm

(1) Pre-processing. Determine the transponder coordinates by acoustic positioning and pre-process all navigation observables, including two-way travel time, sound velocity profile, and pressure data.

(2) Prediction update. Use the dynamic model developed in Section 3.1 to perform a one-step state prediction, yielding the vehicle's predicted position.

(3) Depth constraint. Derive the optimal constraint information as described in Section 3.2 and impose a depth constraint on the predicted position.

(4) Constrained sound velocity. Apply the constrained two-way equivalent acoustic ray tracing algorithm of Section 3.3 to compute the constrained sound velocity and convert time observables into range measurements.

(5) Measurement update. Establish the relationship between range measurements and state variables using the measurement model of Section 3.1, and perform the measurement update.

(6) Adaptive filtering. Employ Sage-Husa adaptive filtering to adjust the measurement noise covariance, thereby reducing the influence of outliers on navigation accuracy.

(7) Smoothing. Apply RTS smoothing algorithm to back-smooth the acoustic-navigation solution and enhance trajectory stability.

4. Experiments and analysis

To assess the performance of the proposed algorithm, we conducted three experiments, including a high-quality data test, a low-quality data experiment, and a dynamic-depth data test. In this experiment, data quality is defined by the number of acoustic signals received from the seafloor transponders. Specifically, when the percentage of epochs receiving at least four acoustic signals exceeds 60% of the total number of epochs, the dataset is considered high-quality; otherwise, it is classified as low-quality data. Details are as follows.

4.1. A high-quality data test

We carried out the test at a depth of about 3000 m in the South China Sea on July 15, 2019, as presented in Fig. 6. The survey vessel was outfitted with various instruments, including acoustic positioning system, gyrocompass, GNSS, pressure gauge and sound speed profiler. Acoustic positioning system is comprised of two primary components: a transducer mounted on the vessel's underside and the five transponders affixed to the seafloor, as shown in Fig. 7. Acoustic positioning system and GNSS are used to measure the acoustic propagation time, as presented in Fig. 8, and the phase center of the GNSS antenna installed on the vessel. The attitude of the ship was obtained by the gyrocompass. The pressure gauge and sound speed profiler are employed to measure the draft of the transducer and the sound speed profile, as

depicted in Fig. 9. The temperature profile of the experimental area is illustrated in Fig. 9(c), and the in-situ salinity ranges from approximately 33.8 ‰ to 34.9 ‰. The sampling intervals of acoustic positioning system, GNSS system, gyrocompass, and pressure gauge are 8, 1, 0.2, and 1 s, respectively.

We selected a high-quality dataset consisting of 525 epochs, in which each epoch had at least four signals received by the transponders. Out of these epochs, 472 epochs received five signals, while only 53 epochs received four signals, as shown in Fig. 9(b). Additionally, the transponder T5 lost a higher number of signals compared to the other transponders according to Fig. 8. The maximum and minimum of acoustic ray incident angles for all epochs are 63.734° and 0.229°, respectively, and the average of acoustic ray incident angles is 39.089°.

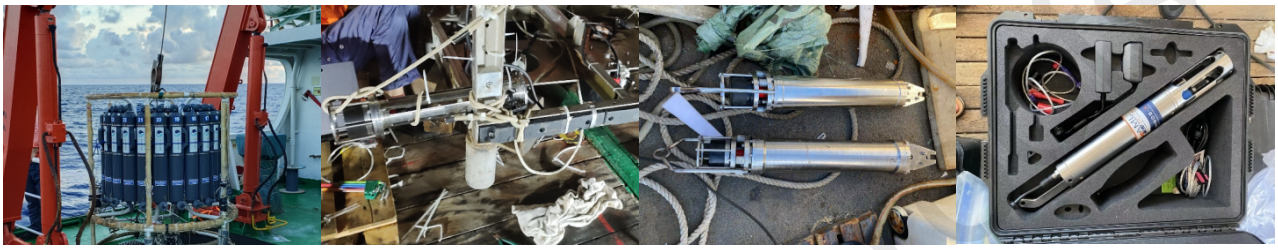

(a) (b) (c) (d)

Fig. 6. Scenes of the ocean test in the South China Sea. (a) water sampler and conductivity temperature depth, (b) transducer installed on the bottom of vehicle, (c) transponders fixed on the seafloor, (d) pressure gauge.

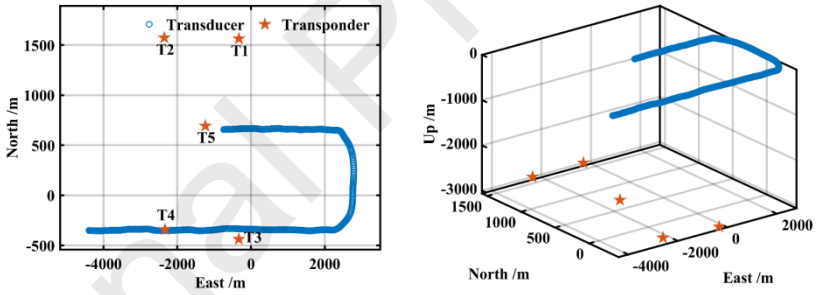

(a) (b)

Fig. 7. Diagram of the vessel surveying trajectories. (a) the 2-D trajectory, (b) the 3-D trajectory.

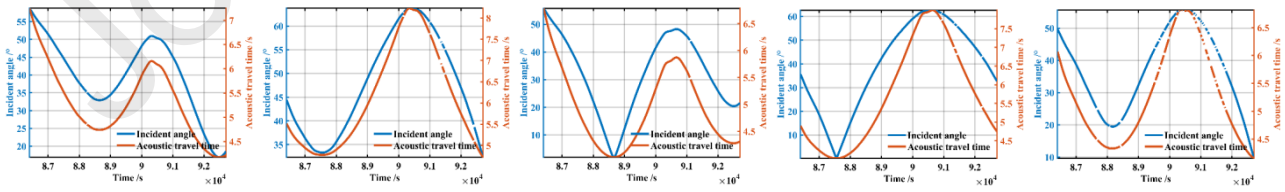

(a) (b) (c) (d) (e)

Fig. 8. Acoustic signal two-way propagation time and acoustic ray incident angles. (a) T1, (b) T2, (c) T3, (d) T4, (e) T5. The absence of lines in the diagrams signifies that the transducer was unable to receive signals from the corresponding transponders.

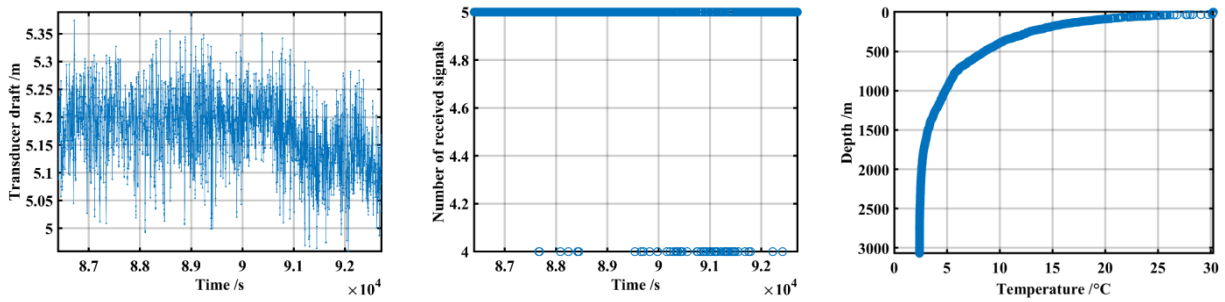

(a) (b) (c)

Fig. 9. Transducer draft and signal reception. (a) draft of the transducer, (b) number of signals received by the transducer, (c) temperature profile of the experimental area.

The acoustic travel distance between the transducer and the transponder can be determined using the acoustic propagation time and the sound speed profile [41]. Subsequently, the transducer's position was calculated by utilizing the acoustic navigation method, which relies on the acoustic propagation distances and the transponder coordinates [42]. The navigation error is defined as the disparity between the transducer coordinates derived from the acoustic navigation algorithm and those obtained by GNSS measurements [43]. Additionally, GNSS directly measures the coordinate of the GNSS antenna, and then deduces the transducer's position based on the ship's attitude and the lever arm distance between the GNSS antenna and the transducer [28].

To assess the navigation performance of the proposed algorithm, the coordinates of the transducers were estimated through three different acoustic navigation methods, namely the traditional method (TM), the traditional method with RTS (RTSM), and the proposed algorithm (Proposed). Herein, TM and RTSM were jointly considered as traditional methods. The obtained navigation results were then analyzed and compared to each other. The navigation errors in the east, north, and up directions for the three methods are illustrated in Fig. 10, while their statistics are presented in Table 2.

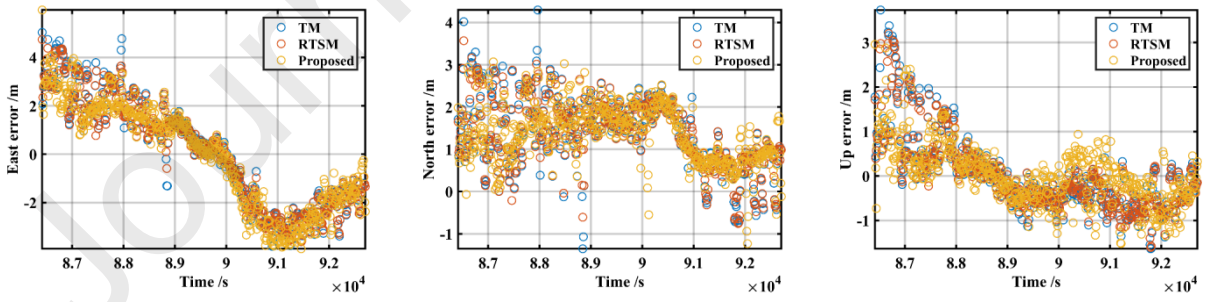

(a) (b) (c)

Fig. 10. Comparison of navigation errors across three methods, namely TM, RTSM, and Proposed. (a) east navigation error, (b) north navigation error, (c) up navigation error. The navigation errors are defined as the difference between the transducer coordinates obtained using GNSS measurements and the acoustic navigation methods.

As shown in Fig. 10, the trends of navigation errors in the east and north directions are similar for the three methods.

However, for certain epochs, the navigation errors of TM and RTSM are noticeably larger than those of Proposed. In the up direction, the navigation errors for the three methods are generally similar in the first half of the measurement period. However, in the second half, the navigation errors of Proposed are lower than those of the other two methods.

Table 2 Statistics of acoustic navigation errors in three directions for the three methods.

Method	Direction	MAE /m	STD /m	RMS /m	RMS-3D /m
	E	1.960	2.229	2.227	
TM	N	1.431	0.829	1.613	2.883
	U	0.632	0.867	0.867	
	E	1.928	2.189	2.187	
RTSM	N	1.408	0.777	1.577	2.821
	U	0.615	0.831	0.831	
	E	1.906	2.163	2.163	
Proposed	N	1.375	0.674	1.516	2.726
	U	0.507	0.673	0.673	

MAE refers to the mean absolute value of the navigation errors, STD represents the standard deviation of the navigation errors, and RMS denotes the root mean square of the navigation errors. RMS-3D is the root mean square error in the east, north and up directions.

Statistics of acoustic navigation errors are shown in Table 2. MAE of Proposed is 2.76%, 3.91%, and 19.78% less than that of TM in the east, north, and up directions, respectively. STD of Proposed is 2.96%, 18.70%, and 22.38% lower compared to that of TM in the three directions, respectively. Moreover, in terms of RMS, Proposed is 2.87% and 6.01% smaller than TM in the east and north directions, respectively, and 22.38% less in the up direction. Compared to RTSM, Proposed has a lower MAE of 1.14%, 2.34%, and 17.56% in the east, north, and up directions, respectively. STD of Proposed is 1.19%, 13.26%, and 19.01% inferior to that of RTSM in these directions, respectively. With regards to RMS, Proposed is 1.10%, 3.87%, and 19.01% beneath RTSM in the east, north, and up directions, respectively.

These results indicate that the proposed algorithm has better accuracy and consistency compared to TM and RTSM in all

three directions. Proposed shows improvements in terms of RMS ranging from 1.10% to 6.01% in the horizontal direction and 19.01% to 22.38% in the vertical direction, with a more significant improvement observed in the vertical direction. Additionally, Proposed demonstrates an improvement of 5.46% and 3.39% in RMS-3D when compared to TM and RTSM, respectively. On average, the proposed algorithm reduces the RMS-3D value by 4.42% compared to the traditional methods.

Table 3 Percentage of epochs in which the proposed algorithm exhibits smaller three-dimensional errors than the traditional methods.

Method	Percentage
TM	66.98%
RTSM	65.65%

In addition, we analyzed the three-dimensional acoustic navigation errors at each epoch and compared the proposed algorithm with the traditional methods. Table 3 summarizes the percentage of epochs in which the proposed algorithm exhibits smaller three-dimensional errors than the traditional methods. Specifically, the three-dimensional errors of the proposed algorithm are smaller than those of TM in 66.98% of epochs, and smaller than those of RTSM in 65.65% of epochs. Furthermore, in epochs where the three-dimensional errors of the proposed algorithm exceed those of the traditional methods, the differences are primarily below 0.5 m. These experimental results indicate that although the improvement of the proposed algorithm is not significant compared with traditional methods, it nonetheless effectively enhances acoustic navigation accuracy in high-quality data test.

In the high-quality dataset scenario, all methods demonstrate low overall positioning errors. The superior performance of the proposed algorithm in this scenario can be attributed to the synergistic effect of the function model, depth constraints, and sound velocity correction. These factors work together to minimize both systematic and random errors in the acoustic measurements. By leveraging high-precision pressure gauge data, the algorithm improves vertical positioning accuracy. Together, these factors explain the observed reduction in navigation error compared to traditional methods.

4.2. A low-quality data experiment

To provide more insight into the performance of the proposed algorithm, we carried out additional validation utilizing datasets of varying quality. The experiment was performed in the waters surrounding Qingdao, China, on August 24th, 2022, as shown in Fig. 11. A schematic diagram of the survey vessel's track and the transponders is illustrated in Fig. 12, where the five transponders were installed on the seafloor at a depth of about 30 m. The survey vessel was outfitted with various instruments, including GNSS, acoustic positioning system, POS MV, pressure gauge, and sound speed profiler. Throughout the experiment, the position of the GNSS antennas, the acoustic propagation time, the attitude of the vessel, the sound speed profile, and the draft of the transducer were recorded using the corresponding instruments, as depicted in Figs. 13 and 14. The environmental parameters of the experimental area, including temperature profile and salinity profile, are shown in Fig. 15.

The vessel was observed for a duration of 36.43 minutes, during which it covered a sailing distance of 2.697 kilometers,

with a total of 1093 observation epochs recorded. Of these epochs, 141 epochs received five signals, 435 epochs received four signals, and 411 epochs received three signals, as illustrated in Fig. 13(b). The incident angles of sound rays were analyzed for all epochs, with the maximum and minimum values being 89.406° and 68.202°, respectively. The average incident angle was found to be 83.425°, as illustrated in Fig. 14. The data presented above indicate that the quality of data in this experiment is inferior to that of the first experiment.

(a) (b) (c) (d)

Fig. 11. Scenes of the ocean experiment in the waters off Qingdao. (a) antennas for various devices, (b) transducers installed on the survey vessel, (c) transponders fixed on the seafloor, (d) survey vessel in operation.

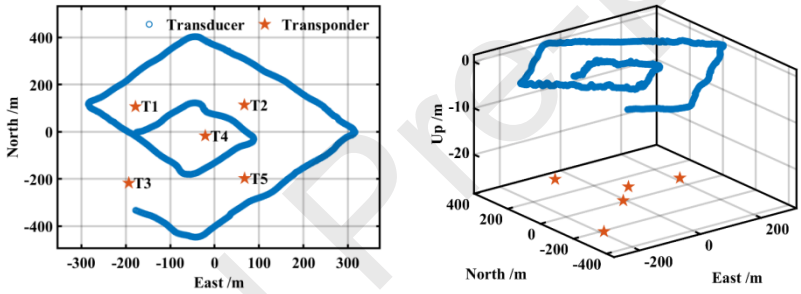

(a) (b)

Fig. 12. Diagram of the vessel surveying trajectories. (a) the 2-D trajectory, (b) the 3-D trajectory.

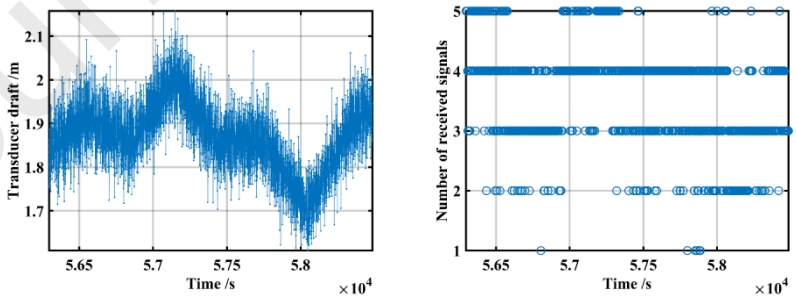

(a) (b)

Fig. 13. Transducer draft and signal reception. (a) draft of the transducer, (b) number of signals received by the transducer.

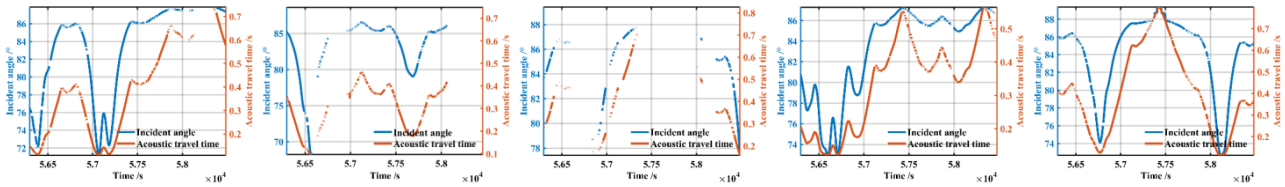

(a) (b) (c) (d) (e)

Fig. 14. Acoustic signal two-way propagation time and acoustic ray incident angles. (a) T1, (b) T2, (c) T3, (d) T4, (e) T5. The absence of lines in the diagrams indicates that the transducer failed to receive signals from the corresponding transponders during the measurement epochs.

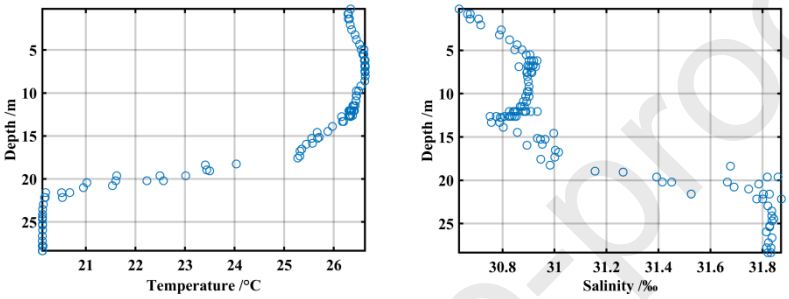

(a) (b)

Fig. 15. Environmental parameters of the experimental area. (a) temperature profile, (b) salinity profile.

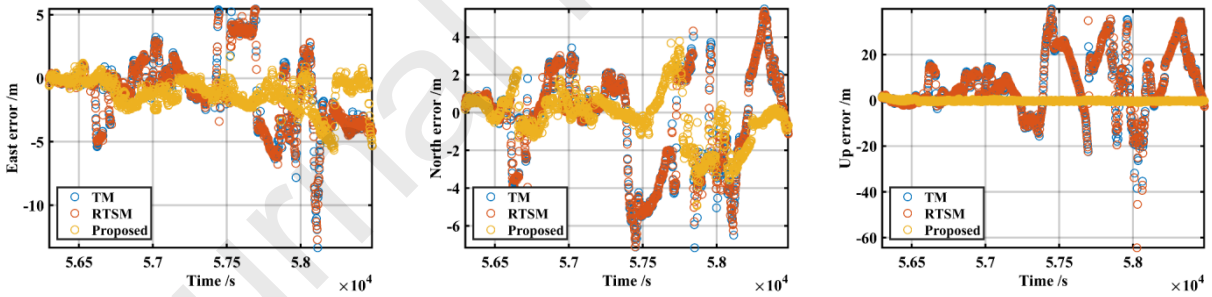

(a) (b) (c)

Fig. 16. Accuracy of the transducer evaluated through acoustic navigation methods, including TM, RTSM, and Proposed. (a) east navigation error, (b) north navigation error, (c) up navigation error.

As depicted in Fig. 16, the mean values of the navigation errors of TM in the east, north and up directions are 2.230, 2.069 and 10.876 m, respectively. Meanwhile, the mean values of RTSM in these directions reaches up to 2.201, 2.050, and 10.779 m, respectively. However, the mean values of Propose in the east and north directions is below 1.233 and 0.969 m, respectively, and it does not exceed 0.314 m in the up direction. Fig. 16 demonstrates that the proposed algorithm achieves better navigation accuracy and stability compared to TM and RTSM, especially in the up direction.

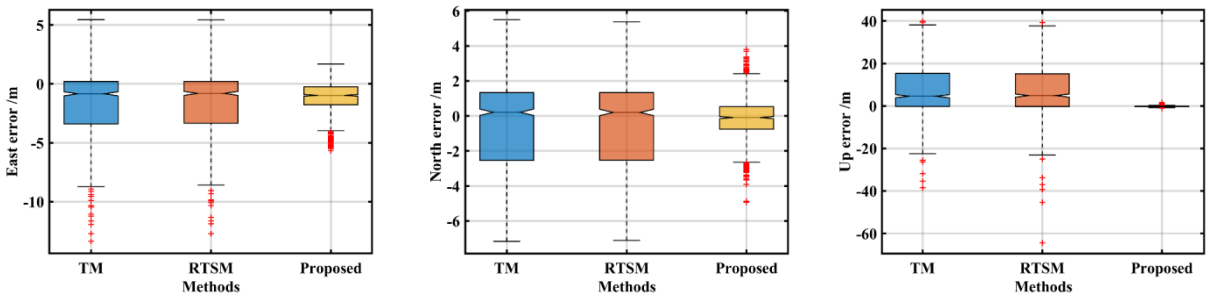

(a) (b) (c)

Fig. 17. Boxplots of acoustic navigation errors in three directions for the three methods. (a) east navigation error, (b) north navigation error, (c) up navigation error.

The central line of the boxplot represents the median of the navigation errors, while the upper and lower lines of the box represent the first and third quartiles (Q1 and Q3), respectively. The difference between Q1 and Q3 is known as the interquartile range (IQR), which represents the middle 50% of the navigation errors.

As presented in Fig. 17, the median values of TM, RTSM, and Proposed in the east direction are -0.843, -0.809, and -0.974 m, respectively. In the north direction, their median values are 0.210, 0.198, and -0.093 m, respectively, and in the up direction, the median values are 4.601, 4.894, and -0.255 m, respectively. Moreover, the IQR values of TM, RTSM, and Proposed in the east direction are 3.594, 3.549, and 1.515 m, respectively. In the north direction, the corresponding IQR values are 3.875, 3.860, and 1.278 m, respectively. For the up direction, TM and RTSM have IQR values of 15.573 and 15.444 m, respectively, while the IQR value of Proposed is 0.284 m. The median absolute value and IQR of Proposed in the north and up directions are less than those of TM and RTSM. In the east direction, although the absolute median value of Proposed is slightly larger than that of TM and RTSM, the IQR of Proposed is significantly smaller than that of TM and RTSM. The above results indicate that the proposed algorithm has a lower navigation error and exhibits smaller variability in all three directions compared to both the TM and RTSM, particularly in the up direction.

Table 4 Acoustic navigation performance of the three methods under various quantities of signals received by the transducer. Unit: m

Num	Epoch	TM			RTSM			Proposed		
		RMS-H	RMS-V	RMS-3D	RMS-H	RMS-V	RMS-3D	RMS-H	RMS-V	RMS-3D
3	411	4.499	15.992	16.612	4.424	15.758	16.368	2.347	0.364	2.375
4	435	3.791	14.589	15.074	3.772	14.511	14.993	1.822	0.373	1.860
5	141	1.450	6.790	6.943	1.416	6.719	6.866	0.982	0.475	1.091

All	1093	3.983	14.513	15.050	3.931	14.510	15.033	2.152	0.383	2.186

Table 4 shows the acoustic navigation performance under different quantities of signals. Num is the number of signals received by the transducer at different epochs. Epoch indicates the number of epochs. RMS-H represents horizontal direction of RMS. RMS-V refers vertical direction of RMS.

Based on Table 4, the proposed algorithm achieves a significant improvement of more than 97% in terms of RMS-V compared to TM and RTSM. The RMS-3D of Proposed decreases by 14.237, 13.214, and 5.852 m over TM when Num is 3, 4, and 5, respectively. Similarly, the RMS-3D values of Proposed show a reduction of 13.993, 13.133, and 5.775 m for the same Num values compared to RTSM. Moreover, Proposed shows an improvement of 85.48% and 85.46% in RMS-3D values across all epochs when compared to TM and RTSM, respectively. The proposed algorithm displays an average reduction of 85.47% in RMS -3D value in contrast to traditional algorithms. These results indicate that the proposed algorithm exhibits significantly smaller navigation error compared to TM and RTSM, with greater improvements observed when the number of signals received by the transducer is small.

Table 5 Percentage of epochs in which the proposed algorithm exhibits smaller three-dimensional errors than the traditional methods.

Method	Percentage
TM	93.78%
RTSM	93.41%

According to Table 5, the three-dimensional errors of the proposed algorithm are smaller than those of TM in 93.78% of epochs and smaller than those of RTSM in 93.41% of epochs. Additionally, even in epochs where the three-dimensional errors of the proposed algorithm exceed those of the traditional methods, the differences are predominantly less than 0.4 m. These experimental results demonstrate that the proposed algorithm substantially reduces acoustic navigation errors in low-quality data experiment, significantly outperforming the traditional methods.

When the dataset quality degrades, the limitations of traditional methods become more pronounced, leading to significant error accumulation. In contrast, the proposed algorithm maintains robust performance. Further analysis of epochs based on the number of received signals reveals that the proposed algorithm's advantage grows as the signal environment worsens. Traditional methods suffer from geometric configuration, resulting in large errors. The incorporation of depth and sound velocity constraints in the proposed algorithm compensates for this weak geometry, preserving positioning accuracy and preventing divergence. As the number of received signals increases, the error reduction provided by the constraints diminishes but still contributes to greater solution stability, particularly in the vertical component.

4.3. A dynamic-depth data test

To further validate that the proposed algorithm is not confined solely to fixed depth mode, but is also equally effective in scenarios where the vehicle operates at variable depths, we performed a dynamic depth experiment. The underwater

vehicle sails along a classic spiral line with a constant speed of 3 knots. Five transponders are deployed on the seafloor with the coordinates T1(500, 0, -500) m, T2(-500, 0, -500) m, T3(0, 0, -500) m, T4(0, 500, -500) m, and T5(0, -500, -500) m in the local Cartesian coordinate system, as presented in Fig. 18. The vehicle operates at seven distinct depths, with a maximum vertical depth variation exceeding 250 meters, as shown in Figs. 18(b) and 19(a). Fig. 19(b) illustrates the number of signals received by the vehicle from the seafloor transponders at each epoch. The sampling intervals of acoustic positioning system, GNSS system, gyrocompass, and pressure gauge are 5, 1, 0.2, and 1 s, respectively. In the experiment, the vehicle descended at a depth change rate of 3 kn during the first two sinkings, 3.5 kn for the following three sinkings, and ascended at 4 kn during the final climb, as presented in Fig. 19(a).

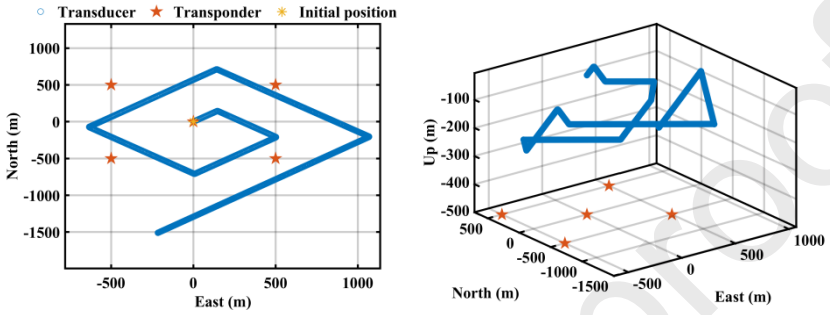

(a) (b)

Fig. 18. Diagram of the vessel surveying trajectories. (a) the 2-D trajectory, (b) the 3-D trajectory.

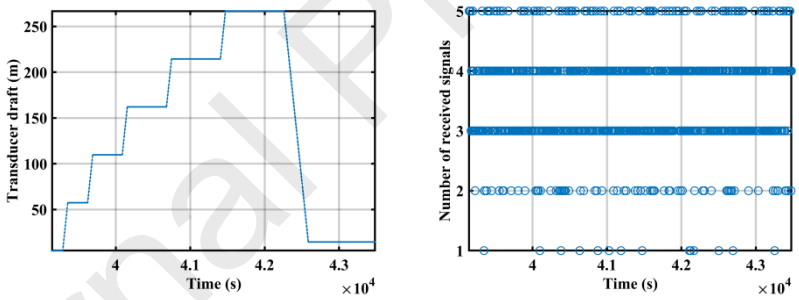

(a) (b)

Fig. 19. Transducer draft and signal reception. (a) draft of the transducer, (b) number of signals received by the transducer.

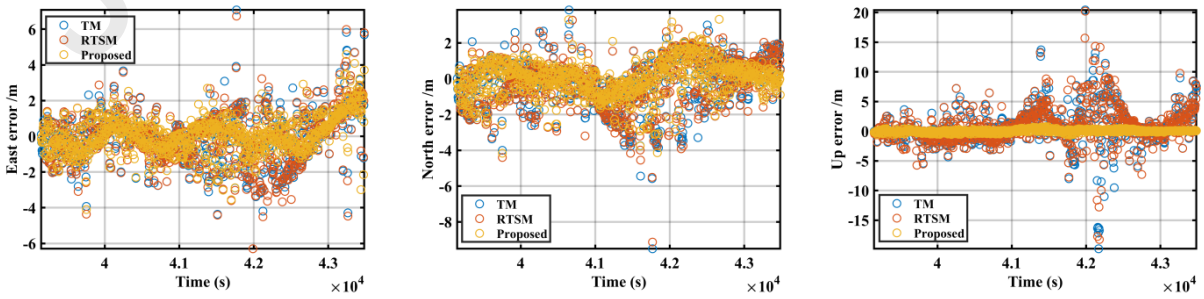

(a) (b) (c)

Fig. 20. Accuracy of the transducer evaluated through acoustic navigation methods, including TM, RTSM, and Proposed. (a) east navigation error, (b) north navigation error, (c) up navigation error.

Table 6 Statistics of acoustic navigation errors in three directions for the three methods.

Method	Direction	MAE /m	STD /m	RMS /m	RMS-3D /m
TM	E	1.074	1.412	1.412	3.882
	N	1.080	1.410	1.429	
	U	2.105	3.268	3.321	
RTSM	E	1.064	1.407	1.407	3.693
	N	1.042	1.341	1.361	
	U	2.021	3.043	3.132	
Proposed	E	0.779	1.020	1.023	1.437
	N	0.742	0.981	0.980	
	U	0.182	0.241	0.242	

Fig. 20 demonstrates that the overall trend in navigation error for RTSM is similar to that of TM across all three directions. Notably, the error markers for the proposed algorithm are significantly more tightly clustered and concentrated much closer to the zero-error baseline, whereas those for TM and RTSM are more widely dispersed and exhibit larger deviations, particularly in the up direction.

Table 6 presents statistics quantifying navigation errors in the east, north, and up directions for three methods. The results show that the MAE, STD, and RMS values for RTSM are all lower than those for TM across the three axes. Specifically, the RMS-3D value for RTSM is 4.87% lower than that for TM, indicating a modest yet consistent improvement in overall accuracy. In contrast, the RMS values in the east, north, and up directions for the proposed algorithm are reduced by 27.55%, 31.42%, and 92.71% relative to TM, and by 27.29%, 27.99%, and 92.27% relative to RTSM, respectively. Moreover, the overall RMS-3D for the proposed algorithm is 62.98% and 61.09% lower compared to TM and RTSM, respectively. These improvements highlight that the proposed algorithm can significantly enhance navigation accuracy, even when the vehicle operates at varying depths.

Table 7 Statistics of acoustic navigation errors at different depth change rates for the three methods. Unit: m

Depth change rates m/s	TM			RTSM			Proposed		
	RMS-H	RMS-V	RMS-3D	RMS-H	RMS-V	RMS-3D	RMS-H	RMS-V	RMS-3D
1.543	2.009	1.140	2.310	1.796	0.966	2.040	1.370	0.205	1.385
1.801	2.087	3.035	3.683	2.074	3.026	3.669	1.316	0.332	1.358
2.058	2.259	4.523	5.055	2.256	4.492	5.027	1.409	0.268	1.435

To further verify the performance of the proposed algorithm, acoustic navigation errors of the three methods at different depth change rates were analyzed, as summarized in Table 7. RTSM consistently exhibits slightly better performance compared to TM across varying depth change rates. Notably, the proposed algorithm significantly outperforms both RTSM and TM, with marked error reductions, especially evident in the vertical direction. Specifically, RMS-V of the proposed algorithm are dramatically lower, approximately 78%-94%, compared with TM and RTSM. These results clearly indicate that the proposed method maintains superior stability and accuracy, even under rapidly varying depth conditions.

The superior performance of the proposed algorithm in the dynamic-depth data test directly results from its adaptive use of pressure gauge constraints and robust sound velocity correction. These features enable accurate real-time tracking of rapid depth changes, resilience to temporary acoustic signal degradation, and maintenance of navigation accuracy, especially in the vertical direction, in highly dynamic underwater environments.

5. Conclusions

To address the limitations of traditional acoustic navigation methods and enhance navigation accuracy, we propose a novel underwater acoustic two-way navigation method based on depth constraint and RTS smoothing. Firstly, it gives a function model of underwater two-way navigation. PDOP is then used to search for the optimal constraint information and constrain the sound velocity calculation and the vertical coordinate of the transducer. Finally, RTS is applied to smooth the navigation results in a backward direction. The proposed algorithm was validated using datasets of varying scenarios, leading to the following conclusions.

(1) The results of the first test demonstrate that the proposed algorithm reduces the RMS-3D value by an average of 4.42% compared to the traditional methods. Furthermore, in the second experiment, the proposed algorithm displays a reduction in the RMS-3D value by an average of 85.47% over the traditional methods. These findings suggest that the proposed algorithm improves navigation accuracy more significantly in the low-quality dataset as opposed to the high-quality dataset.

(2) The RMS-3D values of the proposed algorithm decrease by an average of 14.115, 13.174, and 4.719 m over the traditional methods when Num is 3, 4, and 5, respectively. This observation indicates that the proposed algorithm shows

a more pronounced enhancement in navigation accuracy when the number of signals received by the transducer is lower.

(3) The proposed algorithm exhibits superior accuracy and consistency in the east, north, and up directions in contrast to the traditional methods, with the greatest improvement observed in the up direction. Furthermore, the proposed algorithm is not only limited to fixed depth scenes, but also effectively performs depth constraints when the vehicle operates at different depths.

(4) The proposed algorithm is currently applied to post-processing, while future work will aim to address the challenges of real-time data acquisition, and integration with multi-sensor systems.

References

[1] W. Li, W. Wu, J. Wang, M. Wu, A novel backtracking navigation scheme for autonomous underwater vehicles, Measurement 47 (2014) 496-504. https://doi.org/10.1016/j.measurement.2013.09.022

[2] P. Wu, W. Nie, Y. Liu, T. Xu, Improving the underwater navigation performance of an IMU with acoustic long baseline calibration, Satell. Navig. 5 (2024) 7. https://doi.org/10.1186/s43020-023-00126-1

[3] Z. Jing, Y. Si, Y. Chen, A review of subsea AUV technology, J. Mar. Sci. Eng. 11 (2023) 1119. https://doi.org/10.3390/jmse11061119

[4] A. Karmozdi, M. Hashemi, H. Salarieh, A. Alasty, Implementation of Translational Motion Dynamics for INS Data Fusion in DVL Outage in Underwater Navigation, IEEE Sens. J. 21 (2021) 6652-6659. https://doi.org/10.1109/JSEN.2020.3042902

[5] Y. Zhu, T. Zhang, B. Cui, X. Wei, B. Jin, In-Motion Coarse Alignment for SINS/USBL Based on USBL Relative Position, IEEE Trans. Autom. Sci. Eng. 22 (2025) 1425-1434. https://doi.org/10.1109/TASE.2024.3398018

[6] S. Du, F. Zhu, Z. Wang, Y. Huang, Y. Zhang, A Novel Lie Group Framework-Based Student's t Robust Filter and its Application to INS/DVL Tightly Integrated Navigation, IEEE Trans. Instrum. Meas. 73 (2024) 1-21. https://doi.org/10.1109/TIM.2024.3379400

[7] J. Li, H. Duan, X. Li, Y. Huang, DVL-Aided In-Motion Coarse Alignment for Underwater Vehicles with Latitude Uncertainty, IEEE Trans. Veh. Technol. 72 (2023) 12799-12813. https://doi.org/10.1109/TVT.2023.3274768

[8] Y. Zeng, C. Lu, R. Liu, X. He, C. Rong, M. Liu, Wireless Power and Data Transfer System Using Multidirectional Magnetic Coupler for Swarm AUVs, IEEE Trans. Power Electron. 38 (2023) 1440-1444. https://doi.org/10.1109/TPEL.2022.3214318

[9] L. Luo, Y. Huang, G. Wang, Y. Zhang, L. Tang, An On-Line Full-Parameters Calibration Method for SINS/DVL Integrated Navigation System, IEEE Sens. J. 23 (2023) 30927-30939. https://doi.org/10.1109/JSEN.2023.3330874

[10] B. Xu, H. Zhu, Y. Guo, A robust iterative algorithm for SINS/USBL integrated navigation based on dual hydrophone differential model, Measurement 242 (2025) 115854. https://doi.org/10.1016/j.measurement.2024.115854

[11] Y. Chen, D. Zheng, P.A. Miller, J.A. Farrell, Underwater inertial navigation with long baseline transceivers: A near-real-time approach, IEEE Trans. Control Syst. Technol. 24 (2015) 240-251. https://doi.org/10.1109/TCST.2015.2429613

[12] S. Liu, T. Zhang, J. Zhang, M. Xia, A robust tightly SINS/USBL based AUV localization method aided by dual transponder, Measurement 223 (2023) 113725. https://doi.org/10.1016/j.measurement.2023.113725

[13] A. Tomczak, G. Stępień, T. Abramowski, A. Bejger, Subsea wellhead spud-in marking and as-built position estimation method based on ultra-short baseline acoustic positioning, Measurement 195 (2022) 111155. https://doi.org/10.1016/j.measurement.2022.111155

[14] H.H. Chen, Travel-time approximation of acoustic ranging in GPS/Acoustic seafloor geodesy, Ocean Eng. 84 (2014) 133-144. https://doi.org/10.1016/j.oceaneng.2014.04.015

[15] Y. Liu, T. Xu, J. Wang, M. Li, D. Mu, Z. Gao, An improved method for computing acoustic ray incident angle based on secant method, Appl. Acoust. 205 (2023) 109293. https://doi.org/10.1016/j.apacoust.2023.109293

[16] Y. Liu, J.S. Subirana, T. Xu, J. Wang, W. Yang, S. Zhang, J. Shu, Ultra-fast calculation method of incident angle based on underwater acoustic round-trip positioning, Ocean Eng. 305 (2024) 117998. https://doi.org/10.1016/j.oceaneng.2024.117998

[17] H.H. Chen, C.C. Wang, Accuracy assessment of GPS/Acoustic positioning using a seafloor acoustic transponder system, Ocean Eng. 38 (2011) 1472-1479. https://doi.org/10.1016/j.oceaneng.2011.07.002

[18] R.E. Kalman, R.S. Bucy, New results in linear filtering and prediction theory, J. Basic Eng. 83 (1961) 95-108. https://doi.org/10.1115/1.3658902

[19] Y. Liu, T. Xu, J. Wang, D. Mu, Multibeam seafloor topography distortion correction based on SVP inversion, J. Mar. Sci. Technol. 27 (2022) 467-481. https://doi.org/10.1007/s00773-021-00845-7

[20] S. Zhao, Z. Wang, Z. Nie, K. He, N. Ding, Investigation on total adjustment of the transducer and seafloor transponder for GNSS/Acoustic precise underwater point positioning, Ocean Eng. 221 (2021) 108533. https://doi.org/10.1016/j.oceaneng.2020.108533

[21] Y. Osada, M. Kido, H. Fujimoto, Y. Kaneda, Development of a seafloor acoustic ranging system toward the seafloor cable network system, Ocean Eng. 35 (2008) 1401-1405. https://doi.org/10.1016/j.oceaneng.2008.07.007

[22] L. Zhang, T. Zhang, H.S. Shin, X. Xu, Efficient underwater acoustical localization method based on time difference and bearing measurements, IEEE Trans. Instrum. Meas. 70 (2020) 1-16. https://doi.org/10.1109/TIM.2020.3045193

[23] R. Costanzi, F. Fanelli, E. Meli, A. Ridolfi, A. Caiti, B. Allotta, UKF-based navigation system for AUVs: Online experimental validation, IEEE J. Ocean. Eng. 44 (2018) 633-641. https://doi.org/10.1109/JOE.2018.2843654

[24] J. Wang, T. Xu, Z. Wang, Adaptive robust unscented Kalman filter for AUV acoustic navigation, Sensors 20 (2019) 60. https://doi.org/10.3390/s20010060

[25] J. Shu, T. Xu, J. Wang, Y. Liu, M. Li, An Improved Robust Interacting Multiple Model Algorithm for Underwater Acoustic Navigation, In China Satellite Navigation Conference (CSNC 2022) Proceedings 3 (2022) 503-517. https://doi.org/10.1007/978-981-19-2576-4_45

[26] J. Wang, T. Xu, Y. Liu, M. Li, L. Li, Augmented underwater acoustic navigation with systematic error modeling based on seafloor datum network, Mar. Geod. 46 (2023) 129-148. https://doi.org/10.1080/01490419.2022.2162646

[27] Y. Yang, X. Qin, Resilient observation models for seafloor geodetic positioning, J. Geodesy 95 (2021) 79. https://doi.org/10.1007/s00190-021-01531-7

[28] X. Qin, Y. Yang, B. Sun, The refined resilient model for underwater acoustic positioning, Ocean Eng. 266 (2022) 112795. https://doi.org/10.1016/j.oceaneng.2022.112795

[29] J. Cao, C. Zheng, D. Sun, D. Zhang, Travel time processing for LBL positioning system, 2016 IEEE/OES China Ocean Acoustics (COA), Harbin, China, (2016) 1-5. https://doi.org/10.1109/COA.2016.7535752

[30] Y. Huang, Y. Zhang, B. Xu, Z. Wu, J. Chambers, A New Outlier-Robust Student's t Based Gaussian Approximate Filter for Cooperative Localization, IEEE-ASME Trans. Mechatron. 22 (2017) 2380-2386. https://doi.org/10.1109/TMECH.2017.2744651

[31] Y. Huang, Y. Zhang, B. Xu, Z. Wu, J. A. Chambers, A New Adaptive Extended Kalman Filter for Cooperative Localization, IEEE Trans. Aerosp. Electron. Syst. 54 (2018) 353-368. https://doi.org/10.1109/TAES.2017.2756763

[32] S. Zhao, Z. Wang, K. He, N. Ding, Investigation on underwater positioning stochastic model based on acoustic ray incidence angle, Appl. Ocean Res. 77 (2018) 69-77. https://doi.org/10.1016/j.apor.2018.05.011

[33] Y. Liu, T. Xu, W. Nie, J. Wang, J. Shu, S. Zhang, W. Yang, High-precision LBL/INS Round-trip Tightly Coupled Navigation Based on Constrained Acoustic Ray-tracking and RTS Smoothing, IEEE Trans. Veh. Technol. 73 (2024) 16432-16444. https://doi.org/10.1109/TVT.2024.3416434

[34] F. Yan, Z. Wang, S. Zhao, Z. Nie, Z. Su, W. Li, A layered constant gradient acoustic ray tracing underwater positioning algorithm considering round-trip acoustic path, Acta Geod. Cartogr. Sin. 51 (2022) 31. https://doi.org/10.11947/j.AGCS.2022.20210234

[35] S. Särkkä, Unscented rauch-tung-striebel smoother, IEEE Trans. Autom. Control 53 (2008) 845-849. https://doi.org/10.1109/TAC.2008.919531

[36] S. Liu, X. Zhang, L. Xu, F. Ding, Expectation-maximization algorithm for bilinear systems by using the Rauch-Tung-Striebel smoother, Automatica 142 (2022) 110365. https://doi.org/10.1016/j.automatica.2022.110365

[37] Y. Huang, Y. Zhang, Y. Zhao, L. Mihaylova, J.A. Chambers, Robust Rauch-Tung-Striebel smoothing framework for heavy-tailed and/or skew noises, IEEE Trans. Aerosp. Electron. Syst. 56 (2019) 415-441. https://doi.org/10.1109/TAES.2019.2914520

[38] S.A. Memon, W.G. Kim, M.S. Park, M. Attique, Rauch-Tung-Striebel smoothing linear multi-target tracking in clutter, IEEE Access 10 (2021) 3007-3016. https://doi.org/10.1109/ACCESS.2021.3134987

[39] H. Phillips, Geometrical determination of pdop, Navigation 31 (1984) 329-337. https://doi.org/10.1002/j.2161-4296.1984.tb00883.x

[40] P. Sakic, V. Ballu, W.C. Crawford, G. Wöppelmann, Acoustic ray tracing comparisons in the context of geodetic precise off-shore positioning experiments, Mar. Geod. 41 (2018) 315-330. https://doi.org/10.1080/01490419.2018.1438322

[41] T. Ishikawa, Y. Yokota, S.I. Watanabe, Y. Nakamura, History of on-board equipment improvement for GNSS-A

observation with focus on observation frequency, Front. Earth Sci. 8 (2020) 150. https://doi.org/10.3389/feart.2020.00150

[42] F. Petersen, H. Kopp, D. Lange, K. Hannemann, M. Urlaub, Measuring tectonic seafloor deformation and strain-build up with acoustic direct-path ranging, J. Geodyn. 124 (2019) 14-24. https://doi.org/10.1016/j.jog.2019.01.002

[43] N. Kinugasa, K. Tadokoro, T. Kato, Y. Terada, Estimation of temporal and spatial variation of sound speed in ocean from GNSS-A measurements for observation using moored buoy, Prog. Earth Planet. Sci. 7 (2020) 1-14. https://doi.org/10.1186/s40645-020-00331-5

Acknowledges

The study is funded by National Key Research and Development Program of China (2024YFB3909701), Laoshan Laboratory (LSKJ202205104), and National Natural Science Foundation of China (42388102).

Declaration of interests

☒ The authors declare that they have no known competing financial interests or personal relationships that could have appeared to influence the work reported in this paper.

☐The authors declare the following financial interests/personal relationships which may be considered as potential competing interests: